Localised $Al(OH)_3$ Quantum Dot Passivation for Safe-by-Design Rutile TiO_2 Nanomaterials for UV Protection

Nuwangi P Cooray[a], Rajib Chandra Das[a,b], Philip J Barker[c], Michael LF Lerch[d], Konstantin Konstantinov[a]*

a Institute for Superconducting and Electronic Materials, Faculty of Engineering and Information Sciences, University of Wollongong Innovation Campus, Squires Way, North Wollongong, NSW 2500, Australia

b Illawarra Health and Medical Research Institute, Wollongong, New South Wales 2522, Australia

c School of Science, Faculty of Science, Medicine and Health, University of Wollongong, Wollongong, NSW 2522, Australia

d Centre for Medical Radiation Physics, School of Physics, Faculty of Engineering and Information Sciences, University of Wollongong, Wollongong, NSW 2522, Australia

*Corresponding author e-mail: *konstan@uow.edu.au*

RESULTS

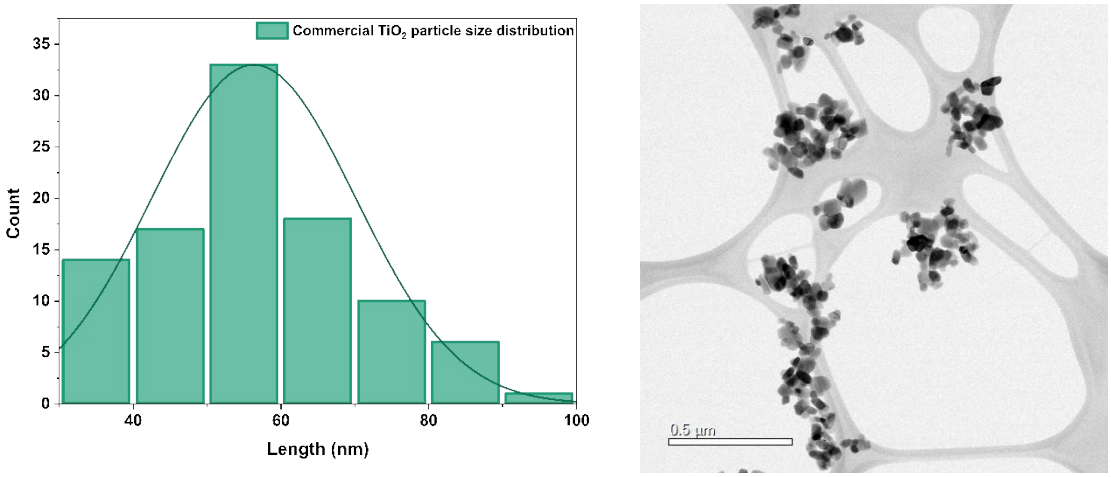

Figure S1 Particle size measurements for commercial TiO_2 nanoparticles with TEM HAADF image showing particle distribution

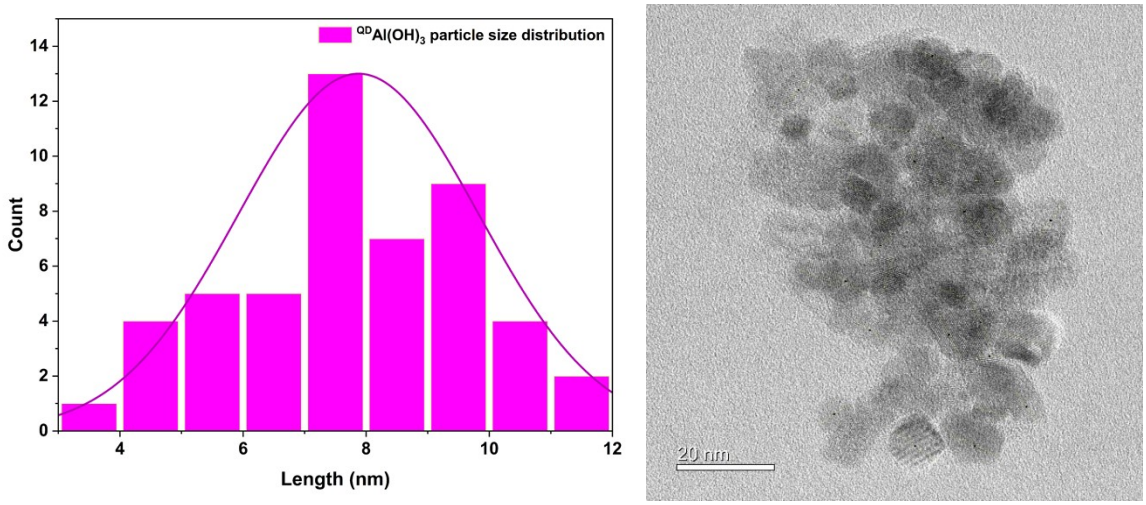

Figure S2 Particle size measurements for $^{QD}Al(OH)_3$ dots with TEM BF image showing particles distribution

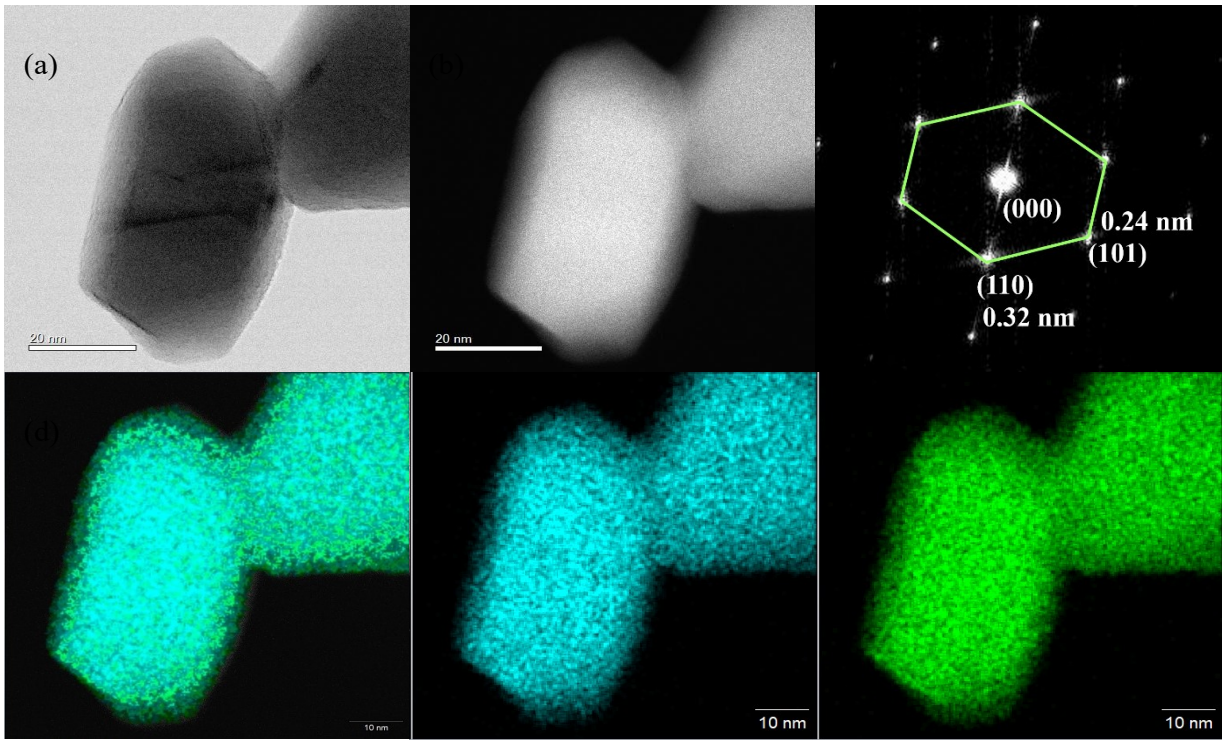

Figure S3 (a) TEM BF, (b) TEM ADF (c) Reduced FFT profile, (d) TEM EDS spectral overlapping map, (e) TEM EDS O elemental map in cyan and (f) TEM EDS Ti elemental map in green for commercial TiO_2.

The specific surface areas and pore volumes of the commercial TiO_2 and $^{QD}Al(OH)_3@TiO_2$ nanocomposites, determined via Brunauer-Emmett-Teller (BET) analysis, are summarised in Table S1.

Table S1 BET surface area and pore volume of the commercial TiO_2 and $^{QD}Al(OH)_3$ @TiO_2 nanocomposites.

Sample	BET surface area (m^2g^{-1})	Pore volume (cm^3g^{-1})
Commercial TiO_2	22.8 ± 0.8	0.0648 ± 0.0086
1.5%wt $^{QD}Al(OH)_3@TiO_2$	18.8 ± 1.0	0.0492 ± 0.0049

3%wt $^{QD}Al(OH)_3@TiO_2$	19.4 ± 1.4	0.0550 ± 0.0071
6%wt $^{QD}Al(OH)_3@TiO_2$	20.7 ± 1.3	0.0660 ± 0.0089

Nitrogen adsorption-desorption measurements were used to evaluate the textural properties of the samples. Pristine TiO_2 nanoparticles exhibit the highest surface area (22.8 ± 0.8 m^2g^{-1}), which decreases upon initial $Al(OH)_3$ quantum dot deposition, reaching a minimum of 18.8 ± 1.0 m^2g^{-1} for

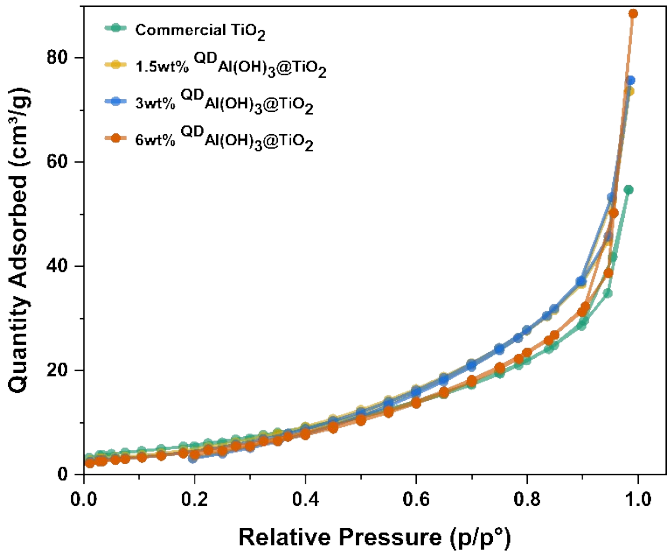

Figure S4 Nitrogen adsorption-desorption isotherms for TiO_2 and $^{QD}Al(OH)_3@TiO_2$ nanocomposites

the 1.5 wt% composite.

The reduction in surface area at low $Al(OH)_3$ loadings is likely due to partial coverage of TiO_2 surface defect sites by $Al(OH)_3$ QDs, effectively decreasing the accessible surface area. However, as the $Al(OH)_3$ loading increases to 3 wt% and 6 wt%, the BET surface area shows a gradual increase, consistent with the formation of $Al(OH)_3$ clusters on the TiO_2 surface as observed in the TEM images. This clustering effect may contribute additional mesoporous structures and surface features, thereby increasing the overall accessible area.

The corresponding nitrogen adsorption-desorption isotherms are shown in Figure S4. All samples exhibit type IV isotherms with H3 hysteresis loops in the relative pressure (P/P_0) range of 0.8-1.0. The type IV isotherms are characteristic of mesoporous materials, while the H3 hysteresis loops suggest the presence of slit-like pores and capillary condensation phenomena, particularly at higher relative pressures.

Pore volume measurements follow a trend similar to that of the surface area, with an initial decrease in the 1.5 wt% composite, followed by a gradual increase as the $Al(OH)_3$ content rises. This further supports the notion that $Al(OH)_3$ encrustation partially blocks the pores at lower loadings but contributes additional porosity through cluster formation at higher concentrations.

In summary, BET analysis confirms that $Al(OH)_3$ surface modification influences both the surface area and pore structure of the TiO_2 nanoparticles, with the observed trends in agreement with the morphological features identified in the TEM analysis.

Thermogravimetric analysis (TGA) of the 6wt% $^{QD}Al(OH)_3@TiO_2$ nanocomposite is presented in

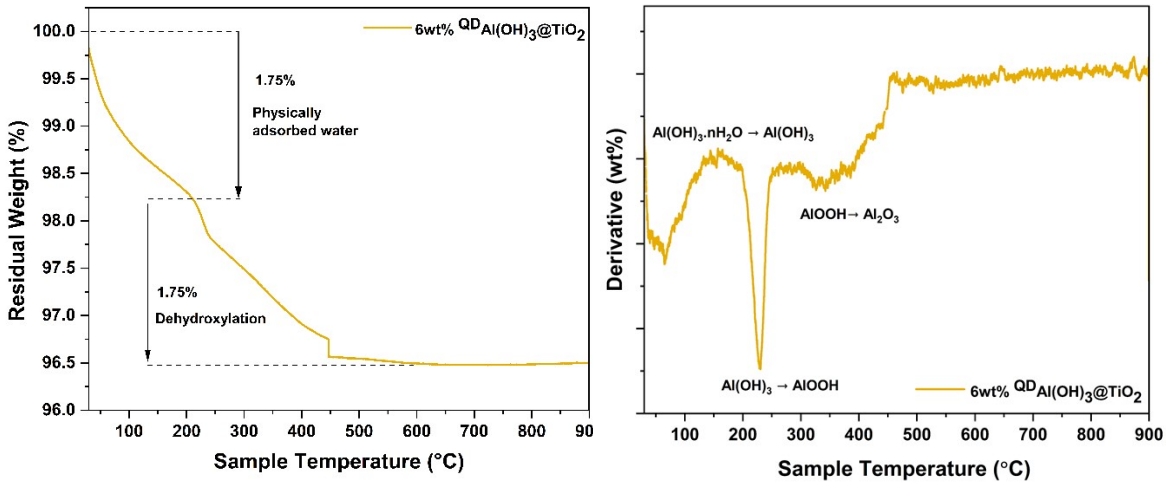

Figure S5 (a)Thermogravimetric analysis and (b) Derivative weight loss for 6%wt $^{QD}Al(OH)_3@TiO_2$

Figure S5.

Thermogravimetric analysis (TGA) of the 6 wt% QD $Al(OH)_3$@TiO_2 nanocomposite is presented in Figure S5. The TGA curve (Figure S5(a)) shows a total mass loss of approximately 3.5% over the temperature range of 30-900°C. Two primary mass loss events are evident: the first, occurring below 150°C, is attributed to the removal of physically adsorbed water, corresponding to approximately 1.75% mass loss. The second event, observed between 150 and 400°C, accounts for an additional 1.75% mass loss and is associated with the dehydroxylation of $Al(OH)_3$ species.

The derivative thermogravimetric (DTG) curve (Figure S5(b)) provides further insight into the thermal transitions. The initial endothermic peak at approximately 95°C corresponds to the desorption of physically adsorbed water from the nanocomposite surface. The prominent endothermic peak centred around 225°C is indicative of the phase transformation from $Al(OH)_3$ (gibbsite) to AlOOH (boehmite)[1]. A subsequent, smaller endothermic event around 350°C is attributed to the conversion of AlOOH to a metastable γ-Al_2O_3 phase.

Although no substantial mass loss is observed beyond 450°C, small fluctuations in the DTG curve around 490°C may suggest the gradual transformation of metastable γ-Al_2O_3 to the more stable δ-Al_2O_3 phase[2-4]. Minor thermal events beyond this point may reflect the continued progression toward the formation of α-Al_2O_3 at elevated temperatures, although this transition is likely incomplete under the experimental conditions due to the limited Al content.

Overall, the thermal analysis confirms the multi-stage phase transformation sequence of $Al(OH)_3$ upon heating and demonstrates the thermal stability of the TiO_2 host structure over the temperature range tested.

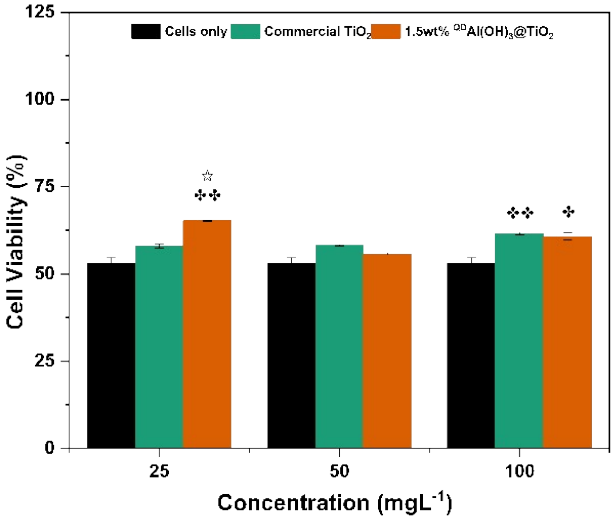

Figure S6 Average HaCaT cell viability with TiO_2 (rutile) and 1.5wt% $^{QD}Al(OH)_3@TiO_2$ at 25, 50 and 100 mg L^{-1} upon 15 min simulated solar irradiation, expressed as percentage of viable cells with respect to IC_0 control. Data are presented as the mean ± SEM (n = 3). Compared to control, ✣ indicates p < .05, ✣✣ indicates p < .01. Compared between the composites ☆indicates p < .05.

Cosmetic performance

Rheological properties

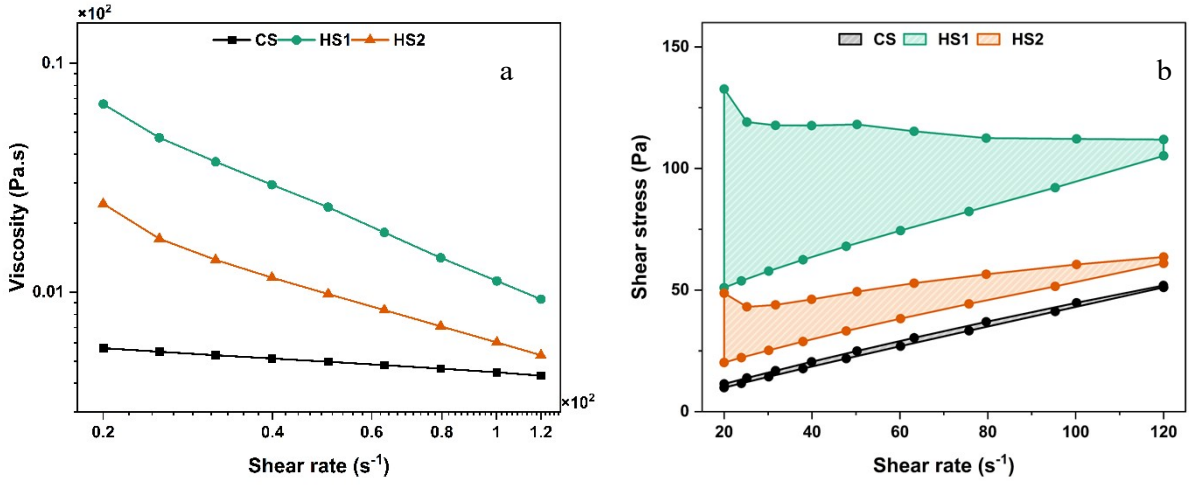

Figure S7 Rheological properties (a) Rheograms and (b) Viscosity measurements of commercial and homemade sunscreens.

The rheological properties of sunscreen formulations play a critical role in their uniformity, spreadability, and overall cosmetic appeal. The relationship between viscosity, shear rate, and shear stress directly influences emulsion stability and application performance. To benchmark cosmetic behaviour, a commercially available sunscreen containing 4.2 wt% nano TiO_2 was evaluated alongside the homemade sunscreens incorporating inorganic nanocomposites.

Figure S7(a) presents the viscosity versus shear rate profiles for the commercial sunscreen and the homemade sunscreen formulations (HS1 and HS2). The homemade sunscreens exhibit higher viscosities at low shear rates than the commercial formulation. This indicates greater structural integrity under minimal mechanical stress. Importantly, all samples demonstrate shear-thinning behaviour-viscosity decreases with increasing shear rate-indicating good spreadability during application. This shear-dependent viscosity is desirable for sunscreen formulations as it facilitates smooth, uniform film formation upon rubbing.

Figure S7(b) shows the shear stress versus shear rate (flow curves) for the same formulations. All samples exhibit nonlinear rheological behaviour characteristic of non-Newtonian fluids. Flow index values (n) calculated using the Ostwald-de Waele model confirm that both commercial and homemade sunscreens are pseudoplastic ($n < 1$). Pseudoplasticity is advantageous for sunscreen emulsions as it supports shear-thinning behaviour, promoting the formation of a continuous and homogeneous protective film on the skin-a critical factor for achieving high SPF values.

The rheograms in Figure S7(b) also reveal thixotropic behaviour in all formulations, evidenced by the hysteresis loops observed during increasing and decreasing shear rate cycles. Thixotropy, which reflects the time-dependent structural recovery of the emulsion, is essential for maintaining uniform coverage after application. The apparent viscosities, flow indices, and thixotropy (hysteresis loop area) are summarised in Table S2.

Table S2 Rheological properties of commercial sunscreens and homemade sunscreens

	Viscosity (Pa.s)	Flow index (n)	Thixotropy ($Pa.s^{-1}$)
CS	0.53 ± 0.04	0.844 ± 0.003	201.34 ± 30.77
HS1	4.59 ± 2.04	0.081± 0.016	3806.53 ± 11.20
HS2	1.72 ± 0.71	0.199 ± 0.032	1218.18 ± 2.27

The homemade sunscreens exhibit higher thixotropy compared to the commercial sunscreen, which may be influenced by the raw materials and the rheological characteristics of the nanocomposite systems used. An optimal thixotropy value is essential for maximum sunscreen efficacy. If thixotropy is too low, the formulation may not spread effectively; if too high, the formulation may not adequately recover its structure, potentially flowing into skin creases and creating uneven coverage. It has been reported that emulsions with excessive thixotropy tend to exhibit reduced SPF values[5,6]. Therefore, a balanced thixotropy is critical for achieving the best UV protection performance.

Overall, among the tested formulations, homemade sunscreen HS2 demonstrated favourable rheological behaviour with good pseudoplasticity, controlled thixotropy, and superior cosmetic performance compared to the other samples.

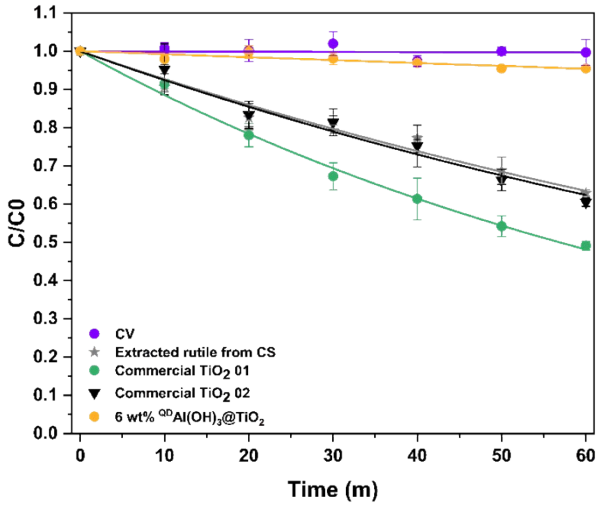

Figure S8 Comparison of photocatalysis in commercial rutile nanoparticles (Commercial TiO_2 01 = Sigma Aldrich, Commercial TiO_2 02 = Tayca MT 100TV

Comparison of photocatalytic activity in commercial rutile nanoparticles

The photocatalytic activity results presented in Figure S8 for different commercial rutile nanoparticles show that QD decoration provided exceptional suppression of photocatalytic activity compared to the currently employed methods.

References

1. Kasprzyk-Hordern, B. Chemistry of Alumina, Reactions in Aqueous Solution and Its Application in Water Treatment. Adv. Colloid Interface Sci. 2004, 110, 19–48. https://doi.org/10.1016/j.cis.2004.02.002.
2. Candela, L.; Perlmutter, D. D. Kinetics of Boehmite Formation by Thermal Decomposition of Gibbsite. Ind. Eng. Chem. Res. 1992, 31, 694–700. https://doi.org/10.1021/ie00003a007.
3. Kim, H.-I.; Lee, S. K. Probing the Transformation Paths from Aluminum (Oxy)hydroxides (Boehmite, Bayerite, and Gibbsite) to Metastable Alumina: A View from High-Resolution ^{27}Al MAS NMR. Am. Mineral. 2021, 106, 389–403. https://doi.org/10.2138/am-2020-7481.
4. Vasile, B. S.; Dobra, G.; Iliev, S.; Cotet, L.; Neacsu, I. A.; Surdu, V. A.; Nicoara, A. I.; Boiangiu, A.; Filipescu, L. Thermally Activated $Al(OH)_3$ Part II — Effect of Different Thermal Treatments. Ceramics 2021, 4, 564–575. https://doi.org/10.3390/ceramics4040040.

5. Gaspar, L. R.; Maia Campos, P. M. B. G. Rheological Behavior and the SPF of Sunscreens. Int. J. Pharm. 2003, 250, 35–44. https://doi.org/10.1016/S0378-5173(02)00462-3.
6. Lee, C. H.; Moturi, V.; Lee, Y. Thixotropic Property in Pharmaceutical Formulations. J. Controlled Release 2009, 136, 88–98. https://doi.org/10.1016/j.jconrel.2009.02.013.